

Wall shear model for mechanical annular polishing

AKAR, Yasemin, JACKSON, Frankie F, MISHRA, Rakesh, ALIYU, Aliyu M, FATAHIAN, Hossein, HUSSAIN, Ameer, WALKER, David, CHEN, Xun, BINGHAM, Paul http://orcid.org/0000-0001-6017-0798, AHUIR-TORRES, Juan and LI, Hongyu

Available from Sheffield Hallam University Research Archive (SHURA) at: https://shura.shu.ac.uk/36375/

This document is the Published Version [VoR]

Citation:

AKAR, Yasemin, JACKSON, Frankie F, MISHRA, Rakesh, ALIYU, Aliyu M, FATAHIAN, Hossein, HUSSAIN, Ameer, WALKER, David, CHEN, Xun, BINGHAM, Paul, AHUIR-TORRES, Juan and LI, Hongyu (2025). Wall shear model for mechanical annular polishing. Journal of Manufacturing Processes, 151, 812-825. [Article]

Copyright and re-use policy

See http://shura.shu.ac.uk/information.html

ELSEVIER

Contents lists available at ScienceDirect

Journal of Manufacturing Processes

journal homepage: www.elsevier.com/locate/manpro





Wall shear model for mechanical annular polishing

Yasemin Akar ^a, Frankie F. Jackson ^{a,*}, Rakesh Mishra ^a, Aliyu M. Aliyu ^b, Hossein Fatahian ^a, Ameer Hussain ^a, David Walker ^a, Xun Chen ^c, Paul A. Bingham ^d, Juan Ahuir-Torres ^c, Hongyu Li ^a

- ^a School of Computing and Engineering, University of Huddersfield, Queensgate, HD1 3DH, UK
- ^b School of Engineering and Physical Sciences, University of Lincoln, LN6 7TS, UK
- ^c School of Engineering, Liverpool John Moores University, UK
- ^d College of Business, Technology and Engineering, Sheffield Hallam University, S1 1WB, UK

ARTICLE INFO

Keywords: Computational fluid dynamics Optical glass material polishing Material removal rate Wall shear stress

ABSTRACT

The applications and the functionalities required for polished glass are countless. Therefore, the polishing process must be designed with extreme care to eliminate surface defects. In this work, the variables affecting the polishing processes for glass are analysed using computational fluid dynamics (CFD) to understand the detailed mechanics of the material removal rate process. The flow field induced by the rotation of the polishing tool, typically used in the annular polishing process, is simulated over a range of tool speeds at various offset (gap between the surface and bonnet) values. Furthermore, to elucidate the additional impact of the particles on the flow field, simulations are performed for both water and abrasive slurry flows. Findings show that reducing the offset distance between the tool and the glass surface significantly increased the shear stress, with the peak value obtained in the region that is in the closest proximity to the rotating tool. The shear stress profile from CFD simulations is compared against experimental profile data for material loss, which displayed good qualitative agreement, especially in the near bonnet region. From the analysis, a power law expression is developed for the estimation of the local shear stress on the workpiece for a given set of process parameters. An R² value of 0.9385 was obtained, showing good correlation between the developed model and CFD results. As such, this equation can be used to estimate shear stress caused by the flowing slurry at various points on the glass surface with confidence during the polishing process.

1. Introduction

Advances in optical technology have heightened the demand for ultraprecision components, where polished glass with exceptionally high surface quality is critical across various optical and industrial applications [1]. There are a host of available processes available for the transformation from a 'raw' blank glass into a finished optical surface, and these can be classified generally into energy-based (ion, laser, or plasma ablation) and abrasive-based processes. Nevertheless, typical processes in optical workshops include:

- i) Grinding basic form, using a CNC machine with a diamond-impregnated hard wheel.
- ii) Smoothing to remove surface and sub-surface damage, using a soft tool.
 - iii) Polishing to deliver a specular surface meeting the texture

specification.

iv) Corrective polishing using metrology feedback to achieve the form specification.

Steps ii) to iv) typically use a water suspension of abrasive particles ('slurry'), which may comprise diamond or aluminium oxide for coarser steps, and almost universally, cerium oxide for polishing glass. In the slurry-based polishing process for glass, the slurry flow characteristics influence the behaviour of the abrasive particles as they traverse the tool/glass interface.

There are a wide variety of available polishing processes, as reviewed recently by Yadav and Das [2]. However, in the context of this paper, there is consideration of the proprietary Precessions TM technique [3], where the tool comprises an inflated spherical membrane (the 'bonnet'), covered with a polishing cloth, and placed at proximity to the workpiece creating a circular 'spot of action', illustrated in Fig. 1. The bonnet is rotated about its axis and precessed about the local normal to the

E-mail address: f.f.jackson@hud.ac.uk (F.F. Jackson).

https://doi.org/10.1016/j.jmapro.2025.07.027

Received 31 January 2025; Received in revised form 30 May 2025; Accepted 7 July 2025 Available online 24 July 2025

1526-6125/© 2025 The Authors. Published by Elsevier Ltd on behalf of The Society of Manufacturing Engineers. This is an open access article under the CC BY license (http://creativecommons.org/licenses/by/4.0/).

^{*} Corresponding author.

Nomenclature			
VF_{CeO_2}	volume fraction of cerium oxide particles [-]		
Re_{ω}	rotational Reynolds number [–]		
τ_w	wall shear stress [Pa]		
μ	dynamic viscosity [Pa·s]		
O_b	bonnet offset distance [mm]		
ρ_{mix}	mixture density [kg·m ⁻³]		
Q	quadrant number (1–4) [–]		
θ	normalised angular position ($\theta = Q/4$) [–] [rad]		
A	Constant from power-law model [–]		
a–d	Constant from power-law model [–]		
r_i	radial coordinate on the workpiece surface [mm]		
N	number of data points [–]		
R^2	coefficient of determination [-]		
RMSE	Root Mean Square Error (dimensionless) [-]		
MAE	Mean Absolute Error (dimensionless [-]		

into this process [6], identified that rather than a chemical interaction contributing primarily to the material removal process, it was the presence of physiochemical or surface-chemical interactions. Through a scanning electron microscope, it was determined that the material removal process in chemical-mechanical polishing was mainly mechanical in nature. Alternatively, a chemistry-aided removal mechanism has been proposed by Kaufman et al. [5]. Presented as a sequential process of formation and removal, resulting in reduced hardness of the surface layer with the removal process occurring via ploughing of the surface. This model was developed in the context of polishing ductile materials such as tungsten (W), where plastic deformation mechanisms are plausible. While not directly applicable to brittle materials like glass, this work introduced foundational ideas about the interplay between surface chemistry and mechanical effects. These mechanisms further analysed by Zhao et al. [7] highlighted the limitations of the study published by Kaufman [5]. The integration of contact mechanics, chemical kinetics, and molecular binding energy was conducted to investigate the material removal process. These computations determined that the ploughing of the surface would not be possible due to the inability for this to occur in dimensions of a molecule. Combining ele-

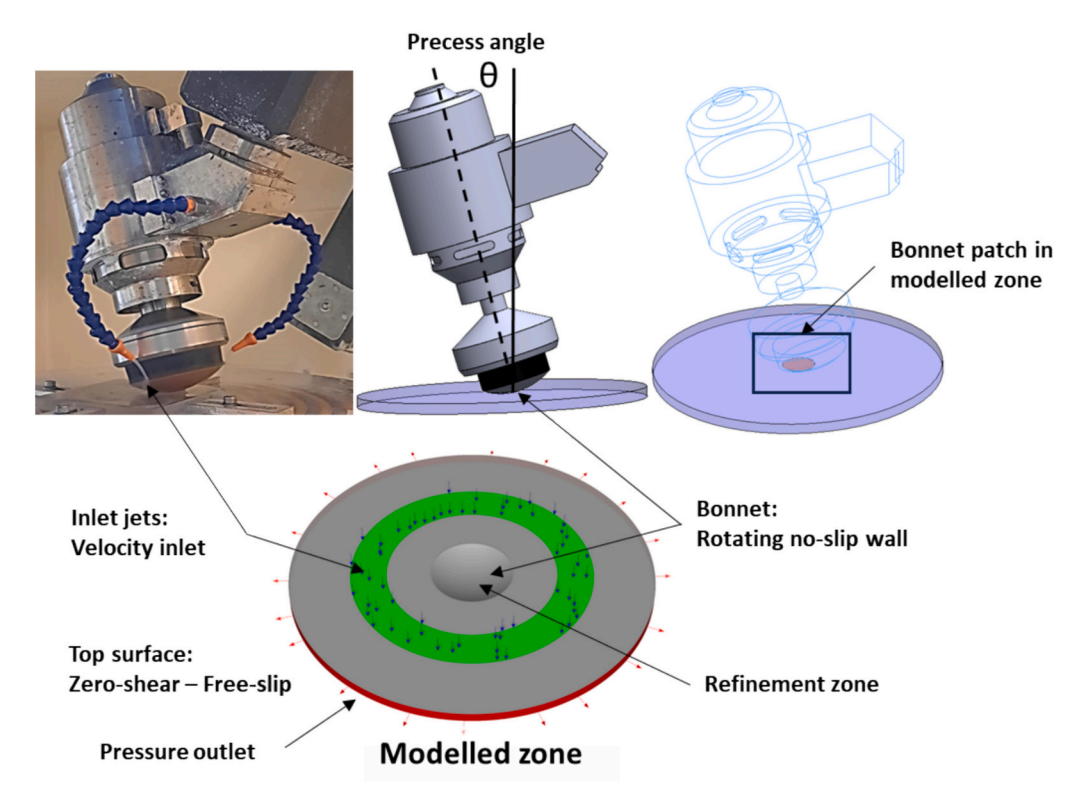


Fig. 1. Physical polishing tool and simplified CAD model of the flow domain.

workpiece surface, delivering a near-Gaussian influence function (removal profile). The bonnet is traversed over the workpiece surface along a pre-programmed toolpath, varying the traverse-speed to modulate the removal-rate (slower traverse removes more material). The key process parameters include the concentration of solid particles in slurry, flow velocity, mechanical and chemical structure of abrasive particles, the bonnet tool diameter, internal pressure, surface characteristics, the compression of the bonnet ('offset'), the tool's motions as it traverses the workpiece, the bonnets rotational speed and the detailed nature of the resulting influence function.

Modelling of material removal mechanisms has found prevalence for the chemical-mechanical polishing process [4,5]. The chemical tooth mechanism presented by Cook [4] highlights the importance of chemical reactions at a surface for material removal. However, investigation ments from work published by Cook et al. [4] and Kaufman et al. [5], Xin et al. [8] postulated that chemical reactions first affect the structure of the work surface, which in-turn is followed by mechanical abrasion. Consequently, the molecules in the modified layer on the work surface are removed by the effect of the strong shear stresses generated by the non-Newtonian slurry flow between the surface and the tool pad.

Multiple process parameters have been highlighted in literature [9] as highly influential to material loss, including lapping pressure, plate rotation speed, plate material, abrasive material grain size, slurry concentration, and slurry flow rate. Marinescu et al. [10], Li et al. [11], and Othman et al. [12] studied the effects of the lapping pressure and plate rotation speed on the MRR. Optimisation of the lapping process determined lapping time and weight provided a greater influence on material loss over lapping speed [12]. The lapping process has also been

optimised to mitigate sub-surface damage [13]. Here it was found that the MRR increases proportionately to abrasive particle size, slurry flow rate, and lapping pressure.

Quantifying the relationship between process parameters and the material removal rate is of vital importance in achieving the required surface finish and minimising error in manufacture. The development of a mathematical model reliant on the Preston equation has aimed to correlate input and outputs in this polishing process [14]. The quantification of process parameters and MRR has also been investigated by Forsberg et al. [15], where the removal rate was examined against plate speed, pressure on the atomically smooth Si (100) surface, comprising mono-, di-, and trihydrides. The study illustrated how varying conditions influence the uniformity and efficiency of the polishing process. Guo et al. [16] investigated the effects of various process parameters on MRR. Abrasive particles' size distribution and polishing pressure were analysed under various vibrating motions. A non-monotonic trend was found between the MRR and applied pressure.

Particle size is a key factor in slurry polishing, with many studies [14,17–23] showing that MRR increases with particle size up to a critical threshold, beyond which further increases have little to no effect or may even reduce effectiveness. Both theoretical and experimental work [19,24] link particle size to wear mechanisms, showing a shift from cutting to sliding actions, and highlighting the need for a wear coefficient that accounts for this change. In addition to particle size, slurry rheology, particularly the volume fraction of abrasive particles, also influences flow behaviour and MRR. Studies [25,26] have shown that viscosity increases with volume fraction and decreases with temperature, although findings vary depending on particle type and shape. These effects are especially significant when considering the combined impact of volume fraction and temperature on slurry performance.

Despite the abundance of research focusing on optimisation, parameter correlation, and polishing process prediction, a universally accepted understanding of the fundamental mechanisms of material removal is still lacking. This gap stems from the complexity of the slurrybased polishing environment, where variables such as abrasive particle interactions, non-uniform distributions, and flow-induced forces significantly influence outcomes but are often oversimplified or overlooked. Prior models tend to assume idealised conditions that do not fully reflect the dynamic, real-world behaviours observed in mechanical annular polishing. These simplifications limit the predictive capability and generalisability of existing approaches. Building on our previous works in modelling solid-liquid flows [27-31], this study addresses these shortcomings by developing a novel model that captures the role of local wall shear stress as a governing parameter in the polishing mechanism. Specifically, the effects of particulate concentration, rotational tool speed, and tool-workpiece offset distance are systematically investigated to quantify their influence on the resulting shear stress distribution at the surface. By coupling multiphase flow modelling with a detailed characterisation of near-wall interactions, this work offers a robust, generalisable framework for predicting polishing performance. This not only advances the fundamental understanding of material removal in complex polishing systems but also supports the development of energy-efficient, high-precision, and cost-effective polishing strategies, addressing key challenges in sustainable manufacturing.

2. Numerical modelling

Using commercially available computational fluid dynamics software, ANSYS Fluent 2024 R2, numerical investigations of the polishing process have been performed. The following sections describe the process of domain creation, numerical configurations, and mesh independence analysis.

2.1. Geometry

For the preliminary numerical investigations, a simplified geometry

Table 1Overview of the simulation parameters.

Parameter	Value
Tool rotational speed Offset Mixture type	1000, 2000 [RPM] 0.5, 1.0 [mm] Single-phase, multi-phase ($CeO_2 = 0.5$ %)

was created consisting of a thin cylindrical flow domain in which the recessed area represents the rotating bonnet. An illustration of the physical polishing tool and simplified flow domain is shown in Fig. 1. To allow a slurry flow of specified volume fraction to enter the domain, an inlet jet area of $0.016~\text{m}^2$ is placed on the top surface. Here an inlet velocity is specified to be 0.0125~m/s to match volumetric flow rate of the physical case of 12~lpm. The remainder of the top surface is defined with specified zero shear (free-slip). The thin outer wall is defined as a pressure outlet and finally, the bottom surface is treated as a no-slip stationary wall.

To model the precess angle (the angle at which the bonnet is tilted before contacting the workpiece), a moving (rotating) wall boundary condition is applied to the recessed area representing the bonnet. This, therefore, requires the specification of the rotation origin and vector. The origin is placed in the centre of the computational domain, with a height (along the *y*-axis) equal to the bonnet radius plus the mechanical offset. Finally, the rotational speed is specified in terms of revolutions per minute.

2.2. Computational settings and boundary conditions

A steady state solution is obtained with the Reynolds Averaged Navier Stokes (RANS) equations. Here, an additional Reynolds stress term is added to the momentum equations, which requires additional modelling consideration. This is referred to as the closure problem and is the subject of turbulence modelling. There are numerous 1- and 2-equation models, each with respective strengths and weaknesses for different modelling applications. For the following simulations, the 2-equation kepsilon shear stress transport method was utilised, as this has been shown to be well suited for modelling adverse pressure gradients and is efficient in terms of computational requirements [32].

For single-phase simulations of liquid water, the fluid properties of density and dynamic viscosity was defined as 998.2 kg/m³ and 0.001003 kg/m•s respectively. For modelling slurry flow, the selection of an appropriate multiphase model is paramount. From preliminary investigations, the Eulerian-Eulerian approach was chosen, with granular properties assigned for one of the phases, as this was found to match closely with experimental measurements [33]. The model was configured with water as the primary phase, and cerium oxide (CeO₂) as the secondary, granular phase, with a density of 7220 kg/m³. For simulation purposes, a monodisperse particle size of 5×10^{-7} was assumed, representing the mean diameter of commercially available cerium oxide polishing particles. This simplification is commonly used in multiphase modelling to isolate key interaction mechanisms while avoiding the added complexity of particle size distribution. For modelling the solid viscosity and granular bulk viscosity, the models of Lun et al. [34] and Gidaspow [35] were used respectively. The packing limit of the CeO₂ was calculated experimentally and was found to be 80.2 % by weight. This experimentally determined packing limit was used to define the maximum solid volume fraction in the Eulerian granular model. This value is essential for accurately capturing particle crowding effects, granular pressure buildup, and interphase momentum exchange in dense slurry regions, particularly near the wall where shear interactions dominate. An overview of the simulation parameters is given in Table 1. The two different offset values of 0.5 and 1.0 mm, in addition to the two rotational speeds of 1000 and 2000 rpm have been used to establish these effects on the flow field, that may be later used for establishing MRR behaviour.

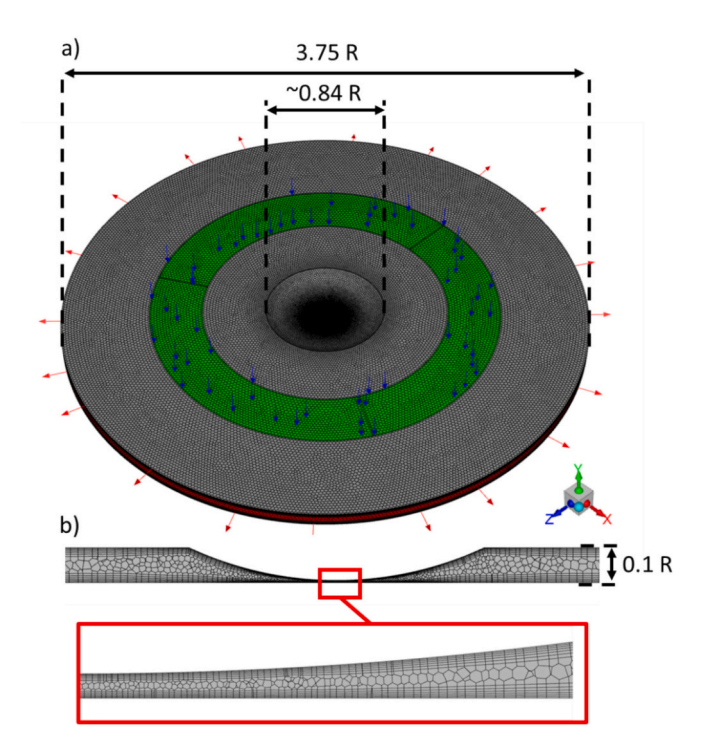


Fig. 2. Generation of mesh in flow domain with local element sizing applied.

2.3. Mesh generation

Polyhedral elements were applied globally due to the high nonuniformity expected of the flow field. In regions in which the smallest length scales were present, such as the 0.5 mm spacing (offset) between the working surface and bonnet, proximity-based sizing control was applied. Inflation layers were added on each of the faces on the top and bottom of the flow domain with a standard growth rate of 1.2, an illustration of which is shown in Fig. 2.

2.4. Mesh independence

To ensure simulation accuracy and balance computational resources, a mesh independence study was performed. The mesh independence study was performed for the case where the bonnet is rotating at 2000 rpm with an offset of 0.5 mm from the surface, as this is assumed to be the most challenging configuration, with the largest velocity gradients and smallest spatial resolution. In addition to monitoring the standard residuals, the simulation convergence was determined through a report of the area-averaged wall shear stress acting on the working surface. Once this value achieved little variation with successive iterations, the simulations were deemed to be suitably converged. A coarse mesh was refined in successive steps with a refinement ratio of two, recording the area-weighted average shear stress at each stage and comparing it to the previous mesh, as illustrated in Fig. 3. The Grid Convergence Index (GCI) was calculated to be 0.9843, which is close to one, indicating satisfactory grid independent results.

A total of four simulations were performed in the mesh study. The wall-averaged shear stress for simulations of different mesh density is recorded and displayed in Table 2. For the subsequent analysis, the chosen mesh comprised of 668,309 elements, as further refinement displayed <5 % difference in the recorded shear stress.

 Table 2

 Results of the wall shear stress for the mesh independence study.

Number of elements	Averaged wall stress [Pa]	Difference [%]
32,408	6.32	_
117,546	6.35	9.87
668,309	6.01	3.79
4,134,788	5.92	1.89

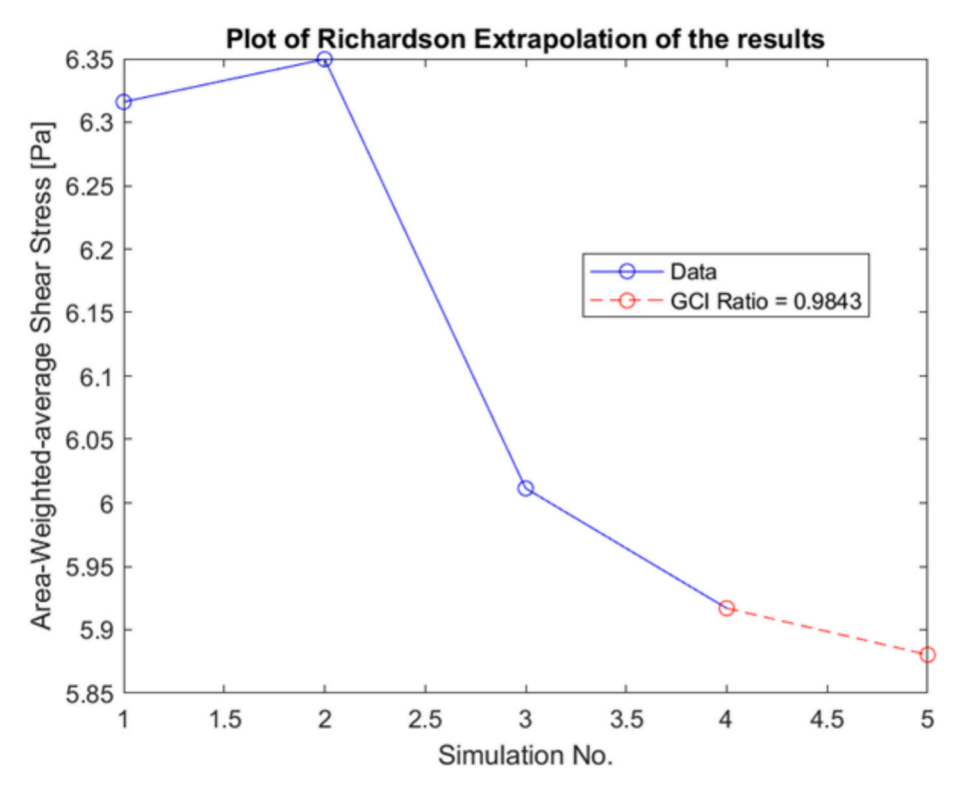


Fig. 3. Illustration of the solver convergence of the face-averaged wall shear stress on the working surface.

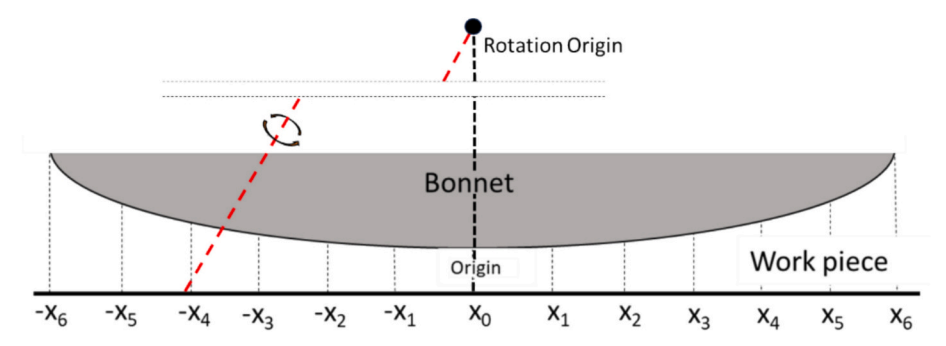


Fig. 4. Illustration of vertical lines between bonnet and surface along x-axis.

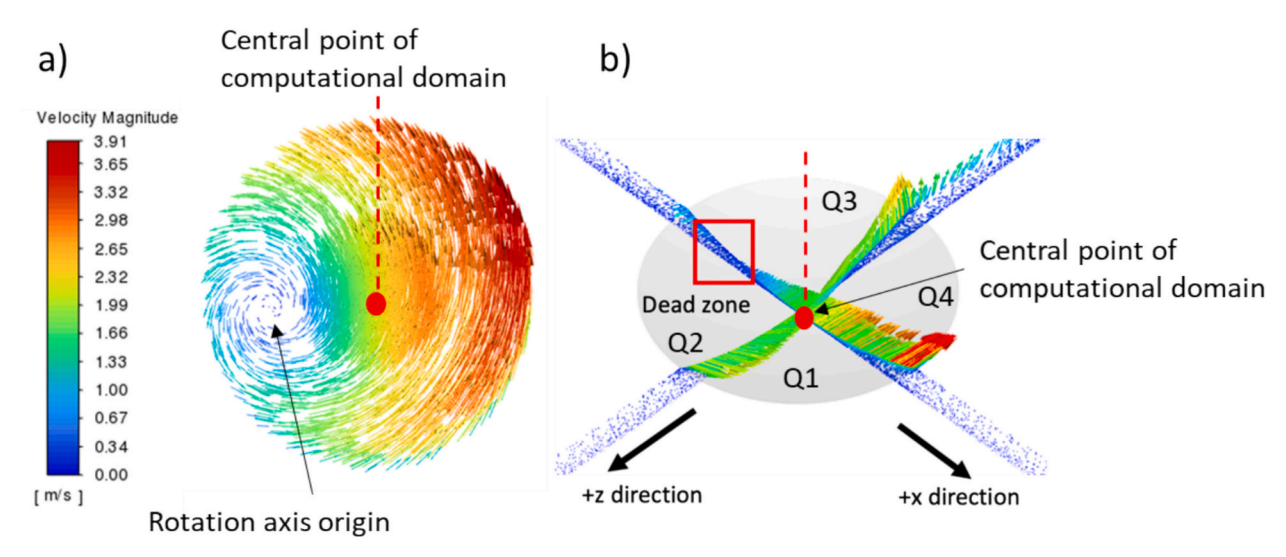


Fig. 5. Illustration of a) the velocity vectors on the bonnet, and b) along the x- and z-axis planes of the domain.

3. Results and discussion

3.1. Single-phase flow

To extract quantitative information on the behaviour of the fluid underneath the bonnet, flow variables were observed at numerous locations along the x- and z-axis extending to the full length of the bonnet section as illustrated in Fig. 4. Here, the marked values are specifying the distance from the origin in either the x- and z-axis and have values of $x_{0,1,\dots,5} = (0 \text{ m}, 0.005 \text{ m}, \dots, 0.025 \text{ m})$ and $x_6 = 0.033 \text{ m}$. At these locations, important information such as the variation in velocity magnitudes is obtained, as explained in the next section.

3.1.1. Velocity magnitude profiles

An illustration of the velocity field caused by the bonnet is shown in Fig. 5(a), (as viewed from the top), here the influence of the precess angle on the applied bonnet rotation is clearly visible. It can be seen that the velocity field is highly non-uniform, and there is significant variation in velocity magnitudes, from the centre of rotation to the bonnet extremity. It can be expected that the effect of this non-uniform velocity field will have considerable impact on wall shear stress on the plate. Keeping in view significant non-uniformity in the velocity field, the flow area has been divided into four quadrants, as shown in Fig. 5(b). Highlighted within is the "Dead zone", where the velocity magnitudes are considerably small, as this is where rotation vector passes through the bonnet.

Figs. 6 and 7 present the normalised velocity magnitude profiles at selected locations shown in Fig. 4. The velocity magnitude is normalised by the angular velocity of the bonnet, ωR , where ω is the rotational speed

and R is the radius of the modelled bonnet patch. To eliminate scale effects, the height is also normalised by the total height of the computational domain. Simulations were conducted for two rotational speeds: 1000 rpm (solid green lines) and 2000 rpm (dashed black lines). Fig. 6a and b shows the velocity profiles for a 0.5 mm offset case, spanning the x- and z-axes, respectively. It should be noted that locations on the negative side of the x- and z-axes are plotted using a reversed axis for better visual representation.

Due to the precessed motion of the bonnet, the velocity distribution along the x-axis in Fig. 6a exhibits significant asymmetry. Three distinct flow regions can be identified: the outer, middle, and central zones. In the outer zone (e.g., locations -x6, -x5, -x4), velocity magnitudes are relatively lower, and the gradients are more diffuse. These characteristics indicate weaker shear forces near the surface, implying a diminished contribution to material removal in these regions. The reduced interaction between the slurry and workpiece surface in the outer zone suggests limited polishing efficiency. In the middle zone (locations -x3, -x2, -x1), the profiles show a clear inflection point, reflecting the transitional flow between the moving bonnet and the stationary substrate. This region is associated with moderate shear development, which likely contributes to consistent but lower-intensity material removal. The central zone, closest to the bonnet's rotational axis, shows the highest velocity magnitudes and steepest gradients. These are most prominent at higher rotational speed (2000 rpm), where the elevated shear stresses at the interface promote aggressive slurry dynamics and abrasive interaction with the workpiece. As the x-axis progresses to the positive direction, similar three-zone behaviour is observed, though the overall velocity magnitudes increase. This is attributed to the asymmetry induced by precession, which biases the flow field and intensifies the

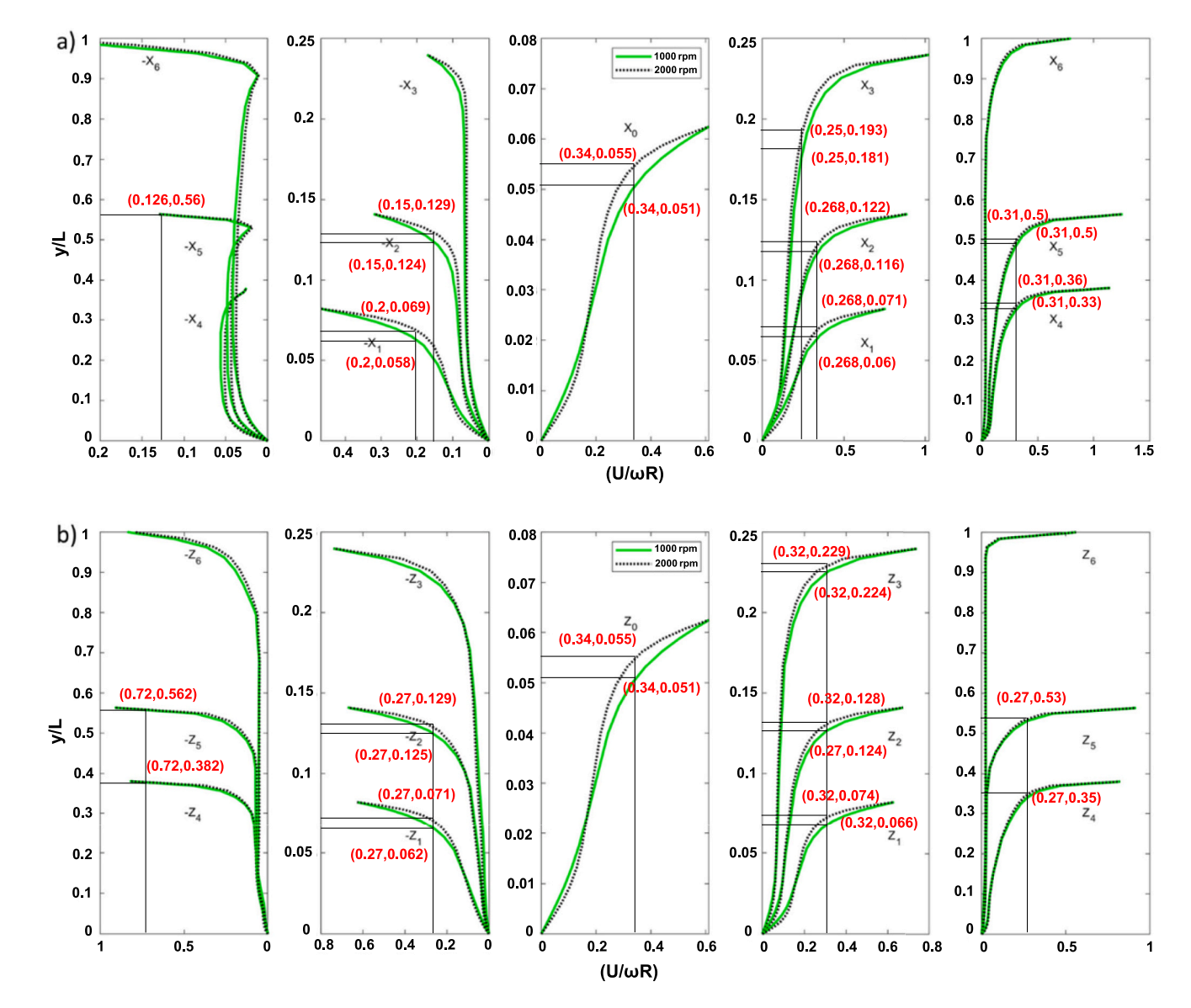


Fig. 6. Non-dimensional velocity profiles for bonnet offset of 0.5 mm. a) Plots spanning the x-axis, and b) plots spanning the z-axis. Solid green lines for 1000 rpm and black dashed lines for 2000 rpm. (For interpretation of the references to color in this figure legend, the reader is referred to the web version of this article.)

contact pressure and shear stress in certain regions. Such variations can explain the non-uniform polishing footprint often observed in experiments and reinforce the importance of controlling offset and rotational speed for uniform surface finish.

Fig. 6b illustrates velocity profiles along the z-axis, where symmetry is more evident due to the axial geometry. In the central z-region (-x3 to x3), dual inflection points are observed, suggesting complex interaction between upward bonnet motion and downward resistance from the workpiece. At the bonnet extremities, higher angular velocity results in sharper velocity gradients near the surface, signifying elevated local shear rates, which are conducive to edge-zone polishing — a critical area in achieving uniform removal profiles. Together, the velocity distributions shown in Figs. 6 and 7 provide insight into the mechanical component of the material removal process. Regions with steeper velocity gradients are associated with higher shear stresses at the slurry-surface interface, which directly correlates with polishing intensity.

To understand the impact of offset on the velocity field, the velocity profiles corresponding to the increased bonnet offset of 1.0 mm are shown in Fig. 7. Similar to Fig. 6a), Fig. 7a) also shows three distinct flow zones. A closer observation reveals that the non-dimensional

heights have almost doubled without significant change in the velocity values. Similar effects are seen in the middle and outer zones. Similar to Fig. 6b), Fig. 7b) displays similar levels of symmetry along the positive and negative z-axis. The speed effects are also found to be similar. From the above we can conclude that there is no significant effect of speed and offset on the flow regime and the nature of parametric dependence remains the same.

3.1.2. Velocity contour plots

To further elucidate the fluid velocity distribution near the workpiece, Fig. 8 presents velocity magnitude contours on a plane 0.1 mm above the bottom surface. The projected axis of rotation is marked with black dots. For a bonnet offset of 0.5 mm at 1000 rpm (Fig. 8a), the velocity field near the model origin is relatively low and widely distributed, with magnitudes peaking at approximately 0.45 m/s. This indicates a more uniform but less intense shearing action across the contact area, suggesting steadier and more consistent polishing. In contrast, at 2000 rpm (Fig. 8b), the velocity near the centre increases sharply to about 0.9 m/s. However, the velocity distribution becomes distinctly asymmetric and highly localised, with sharp gradients forming

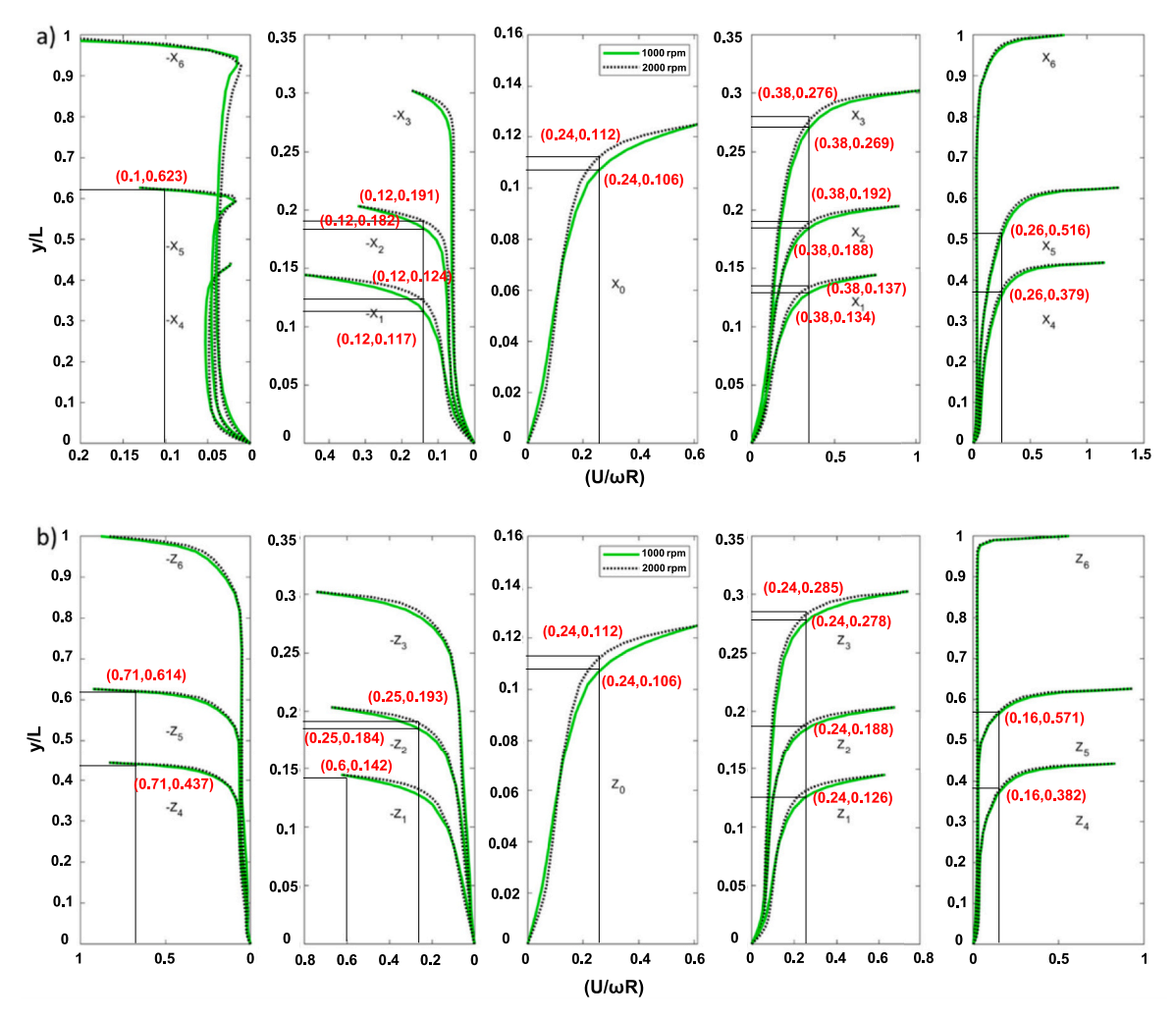


Fig. 7. Non-dimensional velocity profiles for bonnet offset of 1.0 mm. a) Plots spanning the x-axis, and b) plots spanning the z-axis. Solid green lines for 1000 rpm and black dashed lines for 2000 rpm. (For interpretation of the references to color in this figure legend, the reader is referred to the web version of this article.)

around the rotational axis. This non-uniform distribution is indicative of concentrated shear zones, which can cause uneven material removal, particularly in high-velocity pockets. While this may enhance localised polishing efficiency, it compromises the overall uniformity of the process, increasing the risk of surface over-polishing or irregularities.

Fig. 8c and d shows the velocity contours for a larger offset of 1.0 mm at 1000 rpm and 2000 rpm, respectively. At 1000 rpm (Fig. 8c), the field remains moderately uniform with broad velocity gradients and smoother transitions, indicating balanced polishing action. However, at 2000 rpm (Fig. 8d), the asymmetry and concentration of velocity magnitudes intensify, mirroring the trend observed in the lower offset case. This clearly demonstrates that increasing rotational speed disrupts flow uniformity across the work surface, regardless of offset distance, and introduces significant spatial variability into the polishing mechanism.

For the bonnet offset of 1.0 mm, it is clearly observed that the nature of non-uniformity in the velocity field has changed although the velocity magnitudes are in the same range as observed in Fig. 8(c–d). It can be concluded the effect of the bonnet offset at a lower rotational speed on the velocity field is limited. Whereas at a higher velocity, this effect seems significant. It is clear that in each of the four-quadrant identified earlier, the average velocity values vary significantly. A summary indicating the maximum velocity magnitude for each configuration is displayed below in Table 3.

3.1.3. Pressure contour plots

Fig. 9 shows the variation of the pressure field acting on the bottom surface. The "O" symbol is used to illustrate the rotational axis vector intersecting the surface and the "+" symbol shows the model's origin location. It can be clearly seen that the pressure field is highly non-uniform, with low pressure values at the model's origin location, and high-pressure values at outer zones. One noticeable aspect is the creation of zones with low pressures caused by the tool speed and offset distance. Thus, it can be concluded that the desired non-uniformity in the flow field can be managed through a suitable speed and offset distance.

In subfigures Fig. 9c) and d), the pressure contours are displayed for the increased bonnet offset on 1.0 mm for rotational speeds of 1000 and 2000 rpm respectively. The static pressure distribution on the working surface does not show notable change from the one seen at 0.5 mm offset however the magnitude of the static pressure of 1.0 mm offset smaller than that for the 0.5 mm offset case. The above discussion has clearly indicated that both the pressure and velocity fields are affected considerably by the offset and rotational speed. A summary indicating the minimum surface static pressure for each configuration is displayed below in Table 4.

3.2. Multiphase flow

The suspended particles in the mixture are the primary cause of the

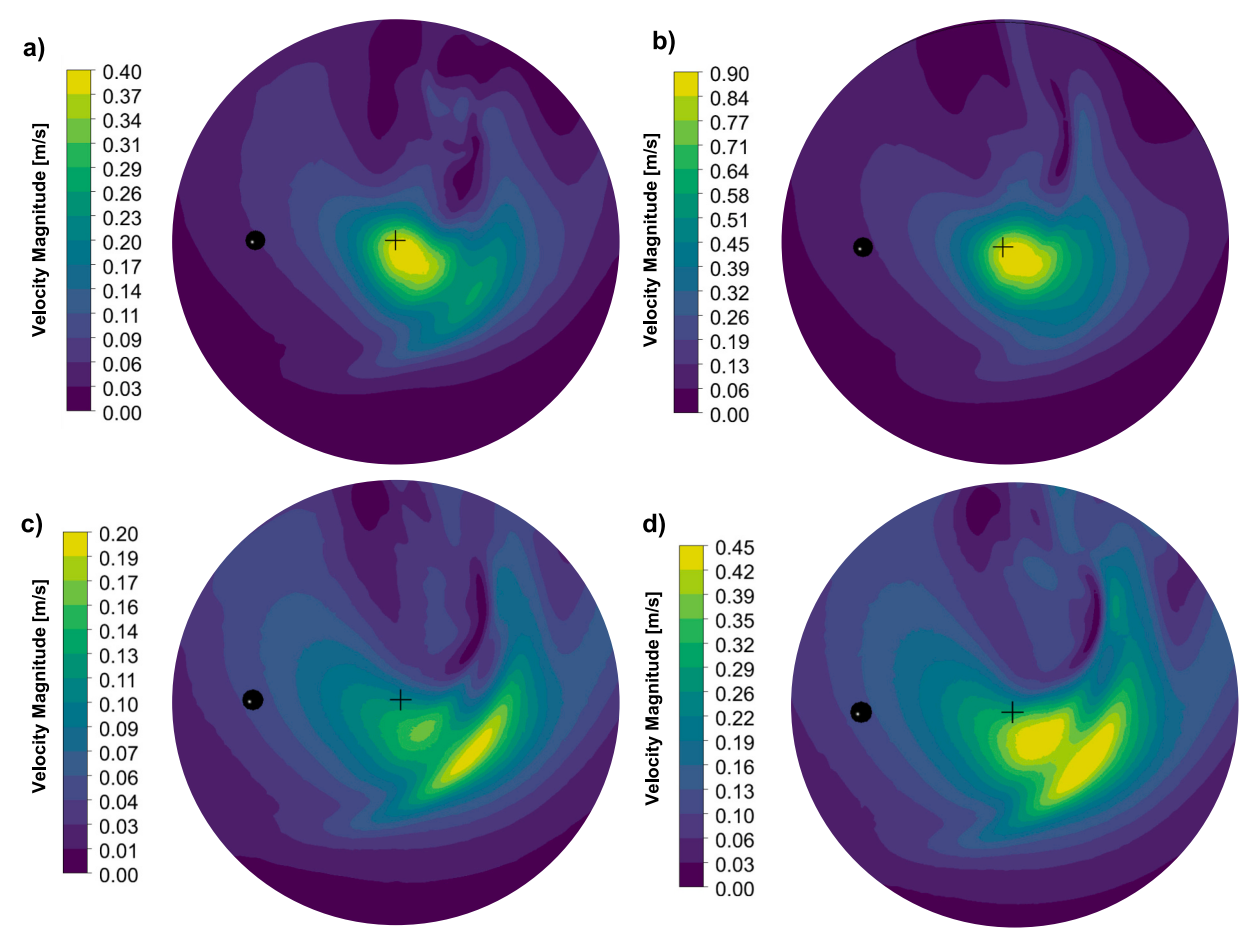


Fig. 8. Velocity magnitude contour plots on a plane 0.1 mm offset from the bottom surface. For a) 0.5 mm offset and 1000 rpm, b) 0.5 mm offset and 2000 rpm, c) 1.0 mm offset 1000 rpm, and d) 1.0 mm offset and 2000 rpm.

Table 3Summary of maximum velocities (m/s) for each configuration.

Offset (mm)	Speed (RPM)	Speed (RPM)	
	1000	2000	
0.5	0.42	1.01	
1.0	0.2	0.48	

wear on the surface. These particles have a higher density than water, and the particle sizes are very small (specified as 0.5 μm). Because of the complex three-dimensional flow field generated by the bonnet, these particles are also expected to have complex motion.

At 2000 rpm, the maximum velocity reaches 1.01 m/s for the 0.5 mm offset (Fig. 10b) and 0.48 m/s for the 1.0 mm offset (Fig. 10d), as opposed to 0.42 m/s and 0.2 m/s at 1000 rpm for the same respective offsets (Fig. 10a and c). Notably, as rotational speed increases, velocity peaks become more sharply confined near the model origin. This increased localisation of high velocities implies that the fluid-induced shear is no longer uniformly distributed across the surface but rather concentrated in narrow regions. Such flow behaviour can exacerbate non-uniform polishing, making it challenging to achieve consistent surface quality.

This effect is quantitatively assessed in Fig. 11, where the normalised maximum velocity and minimum static pressure for each quadrant are compared between single and multiphase cases. The results highlight that the most significant flow non-uniformity arises from high rotational speeds combined with large offsets. Quadrant three shows the largest variation in velocity magnitude under 2000 rpm conditions. Although

static pressure trends appear relatively balanced across quadrants, the velocity data unequivocally demonstrate that higher rotational speeds increase not only the magnitude but also the spatial inconsistency of flow—both of which directly undermine polishing uniformity.

In conclusion, while elevated rotational speeds significantly enhance peak velocities and thus the potential rate of material removal, they introduce strong velocity gradients and pronounced asymmetry in the flow field. This compromises the homogeneity of shear distribution, ultimately reducing polishing uniformity. For applications where surface quality and consistency are critical, optimizing rotational speed is therefore essential to balancing efficiency with control over polishing uniformity. A summary indicating the maximum velocity magnitude for each configuration is displayed below in Table 5.

3.3. Radial wall shear stress profiles underneath bonnet

The wall shear profile was compared against experimental work conducted in the same manner as the investigation conducted by Walker et al. [3]. Fig. 12 presents an overlay of the normalised shear stress profile from the CFD model and the normalised experimental material removal profile. A qualitative agreement is observed within approximately ± 3 mm from the model centre, where both profiles exhibit similar trends in shape and peak location. Beyond this region, deviations occur due to additional flow effects influenced by the bonnet geometry. As both profiles are normalised to their respective peak values, this comparison is intended to highlight general trends rather than exact quantitative agreement.

The shear stress generated on the surface is assumed to be a strong predictor of the material removal on the workpiece. This is predomi-

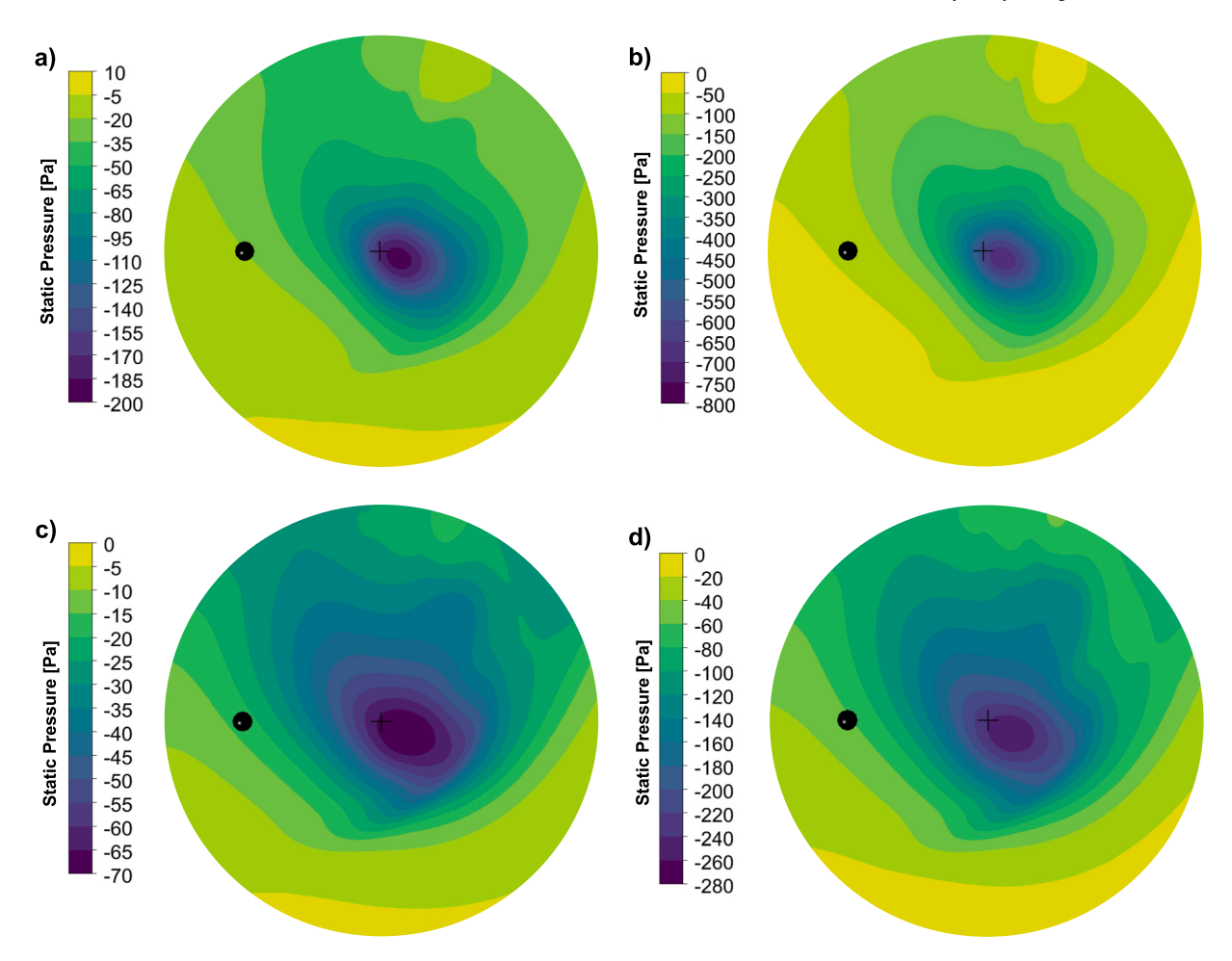


Fig. 9. Pressure contour plots on the working surface. For a) 0.5 mm offset and 1000 rpm, b) 0.5 mm offset and 2000 rpm, c) 1.0 mm offset 1000 rpm, and d) 1.0 mm offset and 2000 rpm.

Table 4Summary of minimum pressures (Pa) for each configuration.

Offset (mm)	Speed (RPM)	
	1000	2000
0.5	-193.8	-687.4
1.0	-71.4	-258.2

nantly influenced by the rotational speed of the bonnet and the offset distance to the glass. For the offset of 0.5 mm, the maximum shear stress acting on the glass was found to be 5.2, and 14.5 Pa for rotational speeds of 1000 and 2000 rpm, respectively. For the offset of 1.0 mm, the maximum shear stress reduced to 2.4 and 6.4 for the 1000 and 2000 rpm respectively. To characterise the distribution of stresses, values were extracted on the surface along the lines shown in Fig. 13. The lines were drawn at 6 radial locations r_i progressively increased until r_i equals the radius of the bonnet. This was done in each of the four quarters that the area under the bonnet was partitioned namely Q1, Q2, Q3, and Q4. The wall shear stress on each line was then averaged to obtain an average or mean wall shear stress value (τ_{wavg}) for that quadrant. For the sections that follow, τ_{wavg} will be used to refer to τ_w for brevity.

Fig. 14 shows the profiles of the dimensionless wall shear stress on the working surface under the bonnet for the single-phase water case. The shear stress was non-dimensionalised by dividing it with $\rho_{mix}v^2$, where $\nu=\omega r$, and ρ_{mix} is the mixture density calculated as $\rho_w(1-VF_{CeO_2})+\rho_{CeO_2}VF_{CeO_2}$. For the single-phase conditions, $VF_{CeO_2}=0$, and $\rho_{mix}=\rho_w$. For all the conditions, the wall shear stress is highest directly

underneath the lowest point of the bonnet at r/R=0. It is seen in Fig. 14 (a) at 1000 rpm and 0.5 bonnet offset that $\tau_w/\rho_{mix}v^2$ is highest in quarter 1 and it progressively decreases away from the bonnet centre. This is expected as the bonnet circumference is farthest from the surface and exerts much less force per unit area on the surface. Fig. 14(b) shows the normalised shear stress values at a bonnet rotational speed of 2000 rpm. Here, the same trend is observed, although the normalised values are smaller, which shows doubling the speed does not result in double the shear stress. For the 1 mm bonnet offset, the effect of rotational speed is less pronounced and the normalised values are approximately two times smaller than the comparable 0.5 mm cases of 1000 and 2000 rpm, in Fig. 14(c) and (d) respectively. The multiphase cases exhibit similar trends as the single-phase conditions in terms of bonnet offset and bonnet rotational speed (Fig. 15).

3.4. Correlation of wall shear stress and process parameters on work surface

It is important to mathematically establish the effect of bonnet offset, rotational speed, and volume fraction of cerium oxide particles at different locations on the surface under the bonnet. To do this, a power law relationship is assumed between the dimensionless wall shear stress as a function of the rotational Reynolds number and other parameters as follows:

$$\frac{\tau_w}{\rho_{mix}v^2} = A Re_\omega^a \left(\frac{O_b}{O_{b_{max}}}\right)^b (1 + VF_{CeO_2})^c \theta^d$$
 (1)

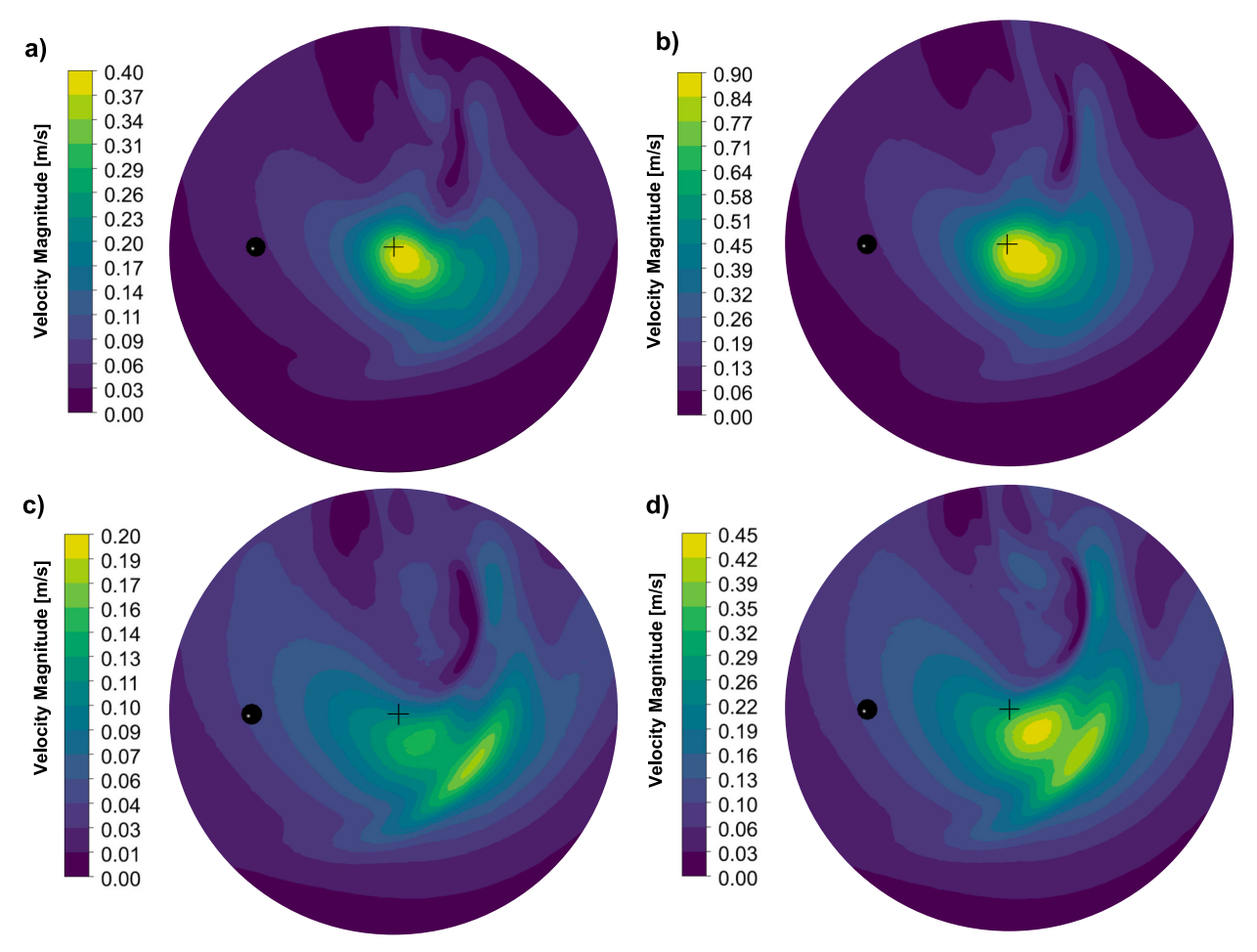


Fig. 10. Velocity contour plots on planes located 0.1 mm away from the working surface. Related cases (a) 0.5 mm offset, 1000 rpm, (b) 0.5 mm offset, 2000 rpm, (c) 1.0 mm offset, 1000 rpm, (d) 1.0 mm offset, 2000 rpm.

where O_b is the bonnet offset distance, and $\theta=Q/4$, where Q is the quadrant, ranging from 1 to 4. The rotational Reynolds number is defined as $Re_\omega=2\rho\omega r^2/\mu_w$. The constant A and indices a–d are determined by non-linear regression analysis using the database of 192 data points. The method of least squares was used, and it was implemented in Microsoft Excel®. For the least squares implementation, Eq. (1) was rewritten by subtracting the LHS from the RHS. As there is never a perfect fit between all pairs of CFD and correlation data points, the result is a remainder or residual for each data point given as:

$$r_{i} = \left[\frac{\tau_{w}}{\rho_{mix}v^{2}}\right]_{CFD,i} - \left[ARe_{\omega}^{a}\left(\frac{O_{b}}{O_{b_{max}}}\right)^{b}\left(1 + VF_{CeO_{2}}\right)^{c}\theta^{d}\right]_{pred,i}$$
(2)

There is no closed-form solution for Eq. (2) and there is existence of an infinite number of solutions. As a result, the best values for coefficient A and indices a-d are those that give the minimum value of the sum of squares of the residuals, S, across the entire CFD database. This minimum that ensures best fit between data and power law model is found by solving the nonlinear least squares minimisation problem:

$$\begin{aligned} \min S &= \sum_{i=1}^{N} r_i^2 \\ &= \sum_{i=1}^{N} \left\{ \left[\frac{\tau_w}{\rho_{mix} v^2} \right]_{CFD,i} - \left[ARe_{\omega}^a \left(\frac{O_b}{O_{b_{max}}} \right)^b (1 + VF_{CeO_2})^c \theta^d \right]_{pred,i} \right\}^2 \end{aligned}$$
(3)

where N is the number of data points in the databank. Eq. (3) is solved

iteratively using the evolutionary algorithm in Microsoft Excel's Solver® add-in. Initial values for a–d were given, and these were carefully chosen to help the algorithm converge easily and to a solution with realistic regression coefficients. The following relationship was hence obtained:

$$\frac{\tau_{w}}{\rho_{mix}v^{2}} = \frac{57353}{\theta^{0.53}Re_{\omega}^{1.04} \left(\frac{O_{b}}{O_{b_{max}}}\right)^{1.34} \left(1 + VF_{CeO_{2}}\right)^{0.47}} \tag{4}$$

Fig. 16 shows that this equation gives a good agreement with the CFD data and can be used to predict the shear stress on the working surface for a given rotational speed, the volume fraction of CeO_2 , and bonnet offset an any location (r, θ) underneath the bonnet.

More than 99 % of the new correlation's values were within ± 1 standard deviation error bands. Statistical error metrics were calculated by comparing the model's predictions with CFD results, yielding a Root Mean Square Error (RMSE) of 0.001, a Mean Absolute Error (MAE) of 0.002 and a correlation coefficient (R² value) of 0.9385. These results indicate that the correlation has good predictive capability within the process conditions studied.

4. Conclusions

In this work, a detailed computational investigation of the mechanical annular polishing process was conducted to explore the influence of key process parameters—namely, tool rotational speed, offset distance, and abrasive particle concentration—on the resulting flow behaviour and wall shear stress distribution. Employing a multiphase Eulerian CFD framework, the study assumes and verifies that wall shear stress is a

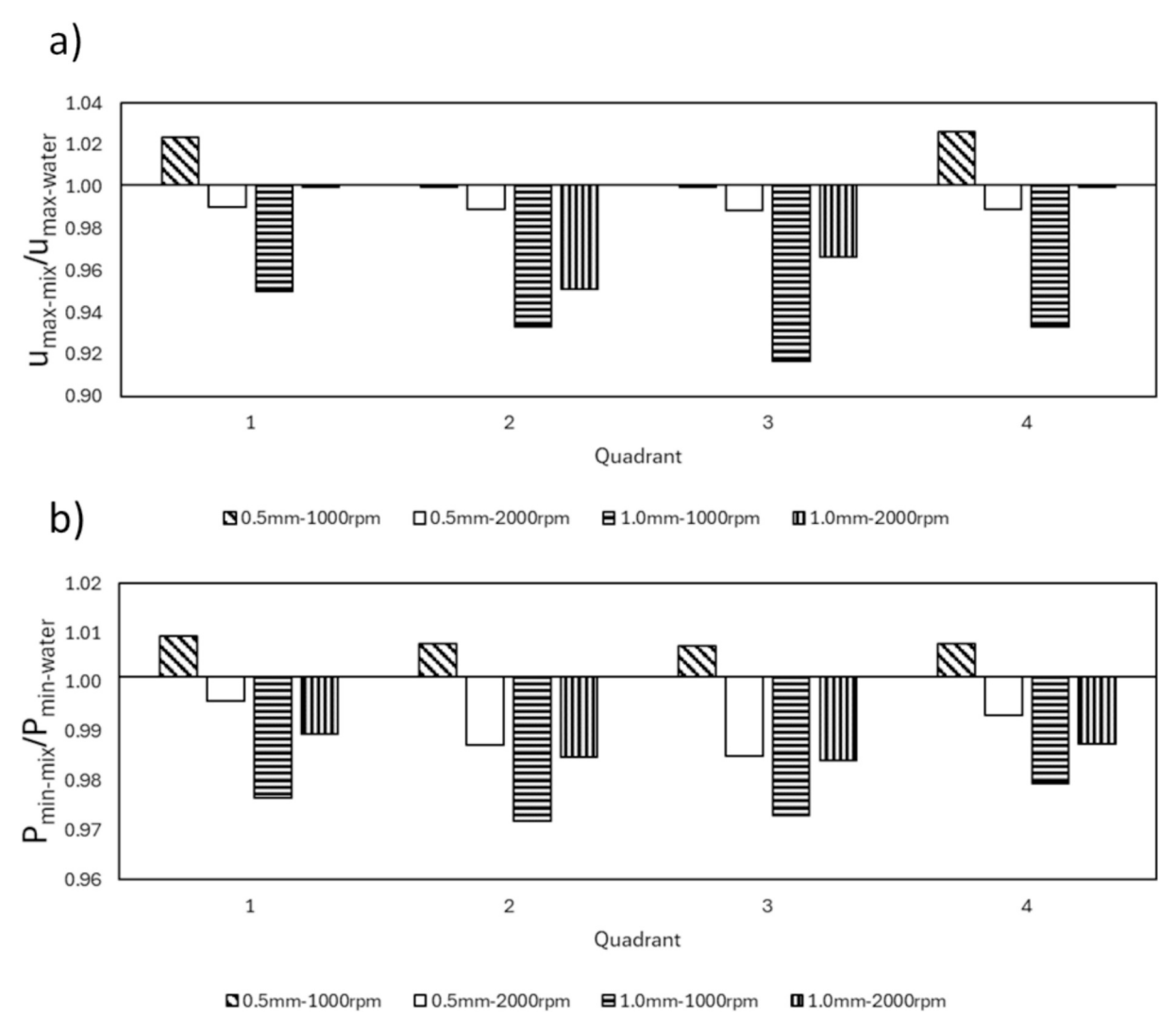


Fig. 11. Normalised values of a) velocity and b) pressure in each quadrant.

Table 5Summary of maximum velocities (m/s) for each configuration — multiphase.

Offset (mm)	Speed (RPM)	
	1000	2000
0.5	0.43	1.0
1.0	0.19	0.48

robust indicator of MRR, both in terms of magnitude and spatial distribution. Comparisons with experimental profiles show strong agreement, reinforcing the validity of this assumption and confirming the relevance of shear stress as a predictor of polishing effectiveness.

Through systematic variation of input parameters and analysis of the resulting flow fields, the study reveals that increased rotational speed significantly elevates the velocity field and amplifies shear stress magnitudes on the workpiece surface. Likewise, reducing the offset between tool and workpiece enhances local shear intensities, especially in regions directly under the bonnet where contact is closest. These findings highlight the critical role of geometric and kinematic configurations in controlling polishing uniformity and efficiency.

Crucially, this work presents a novel predictive model in the form of a power-law expression that quantifies wall shear stress as a function of flow dynamics, slurry composition, and geometric arrangement. The power law model was found to have an $\rm R^2$ value of 0.9385 when

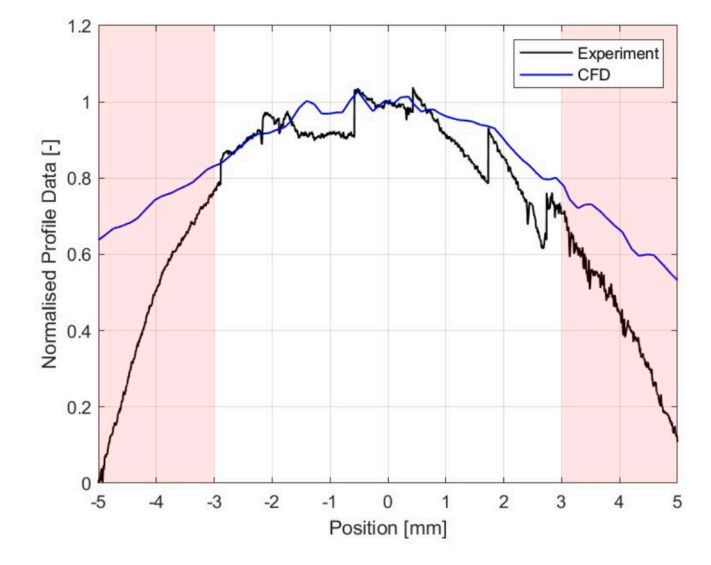


Fig. 12. An overlay of the shear stress contour and the positive offset profile data acquired through experimentation.

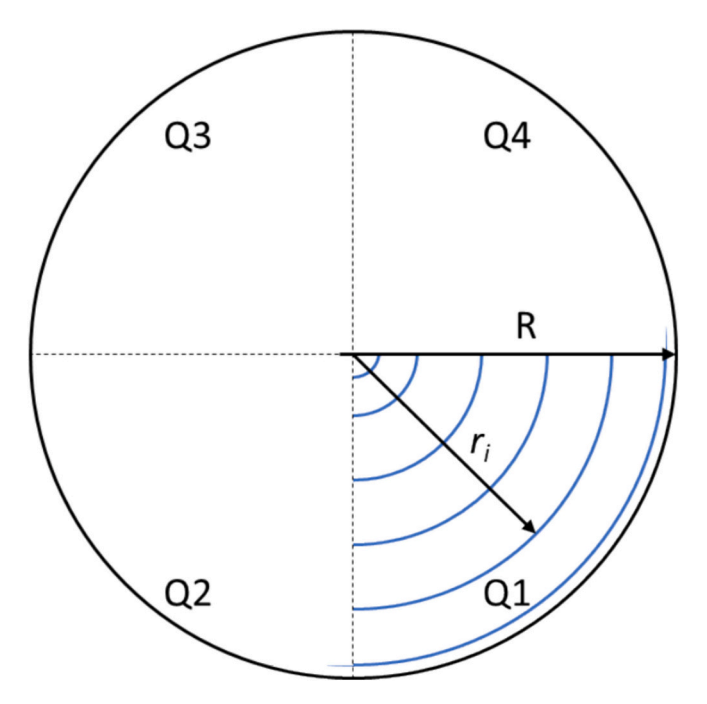


Fig. 13. Illustration of data extraction locations on the surface under the polishing bonnet.

compared to the CFD results, demonstrating a good agreement between

predicted and modelled shear stress values. This model offers a generalisable and physics-based framework for predicting local MRR across varying conditions, with direct applicability to process optimisation in industrial contexts. By capturing the complex fluid–solid interactions in a multiphase slurry environment, this study not only contributes to the mechanistic understanding of the polishing process but also advances the development of data-driven, energy-efficient, and high-precision surface finishing strategies.

A key avenue for future research is the integration of machine learning (ML) with physics-based models to enable real-time, intelligent process optimisation. ML models could be trained on CFD-generated data to predict shear stress distributions and material removal rates across a broader range of process conditions, significantly reducing computational costs and improving decision-making in real-time. Additionally, the range of input parameters should be expanded. Factors like slurry viscosity, particle size distribution, temperature effects, tool geometry, and material properties should be considered in future studies. By incorporating these, a more comprehensive optimisation framework could be developed, enhancing the predictive power of ML models, and enabling a hybrid digital twin approach for continuous process improvement in polishing applications.

CRediT authorship contribution statement

Yasemin Akar: Writing – original draft, Software, Methodology. Frankie F. Jackson: Writing – review & editing, Validation, Software. Rakesh Mishra: Writing – review & editing, Supervision, Software. Aliyu M. Aliyu: Writing – review & editing, Methodology, Formal analysis. Hossein Fatahian: Writing – review & editing, Software.

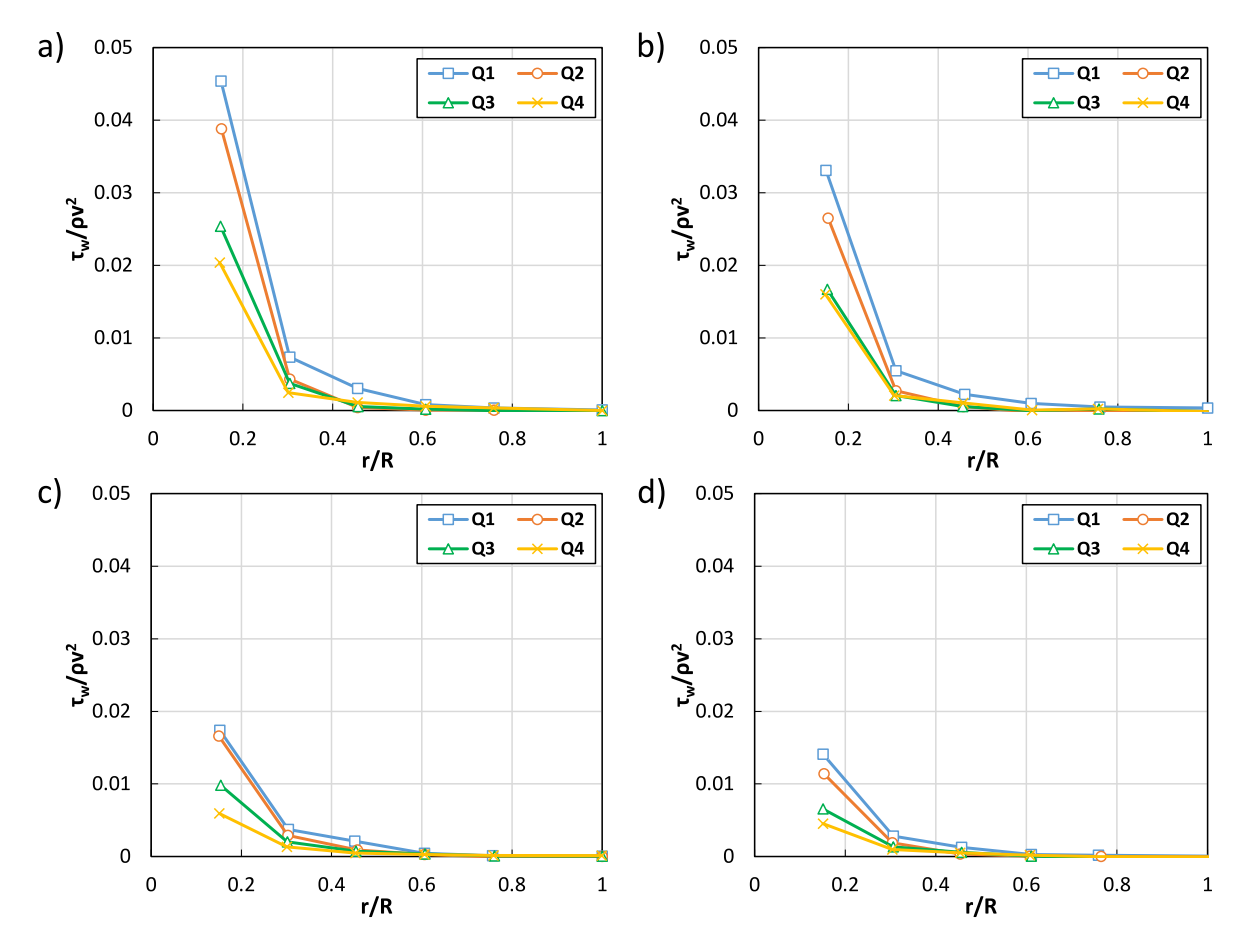


Fig. 14. Radial profiles of non-dimensional wall shear stress on the surface for the four quarters under the polishing bonnet for the single-phase water case. For a) 0.5 mm bonnet offset and 1000 rpm bonnet rotational speed, b) 0.5 mm bonnet offset and 2000 rpm bonnet rotational speed, c) 1.0 mm bonnet offset and 1000 rpm bonnet rotational speed, and d) 1.0 mm bonnet offset and 2000 rpm bonnet rotational speed.

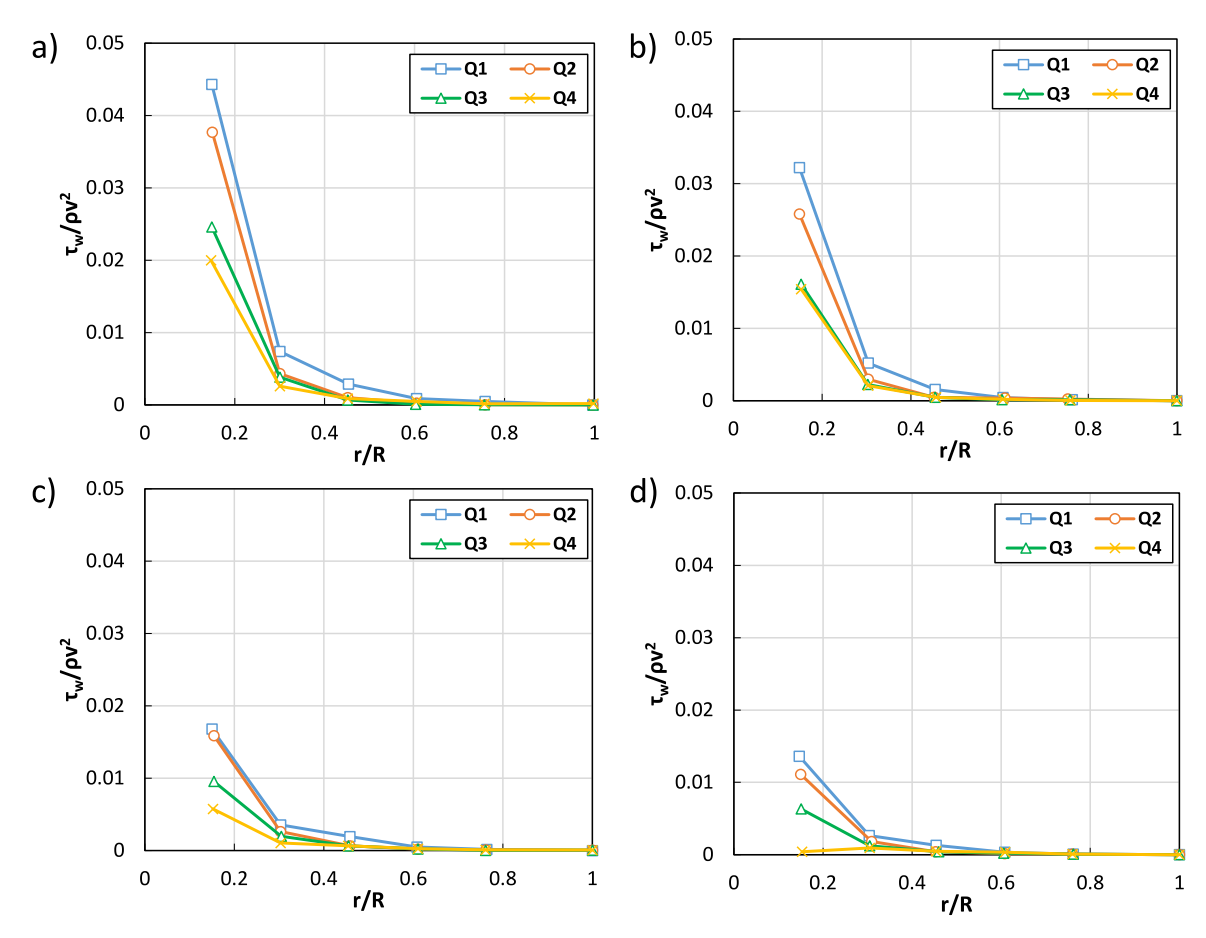


Fig. 15. Radial profiles of non-dimensional wall shear stress on the surface for the four quarters under the polishing bonnet for the multiphase-phase case with 0.5 % volume fraction of cerium oxide particles. For a) 0.5 mm bonnet offset and 1000 rpm bonnet rotational speed, b) 0.5 mm bonnet offset and 2000 rpm bonnet rotational speed, c) 1.0 mm bonnet offset and 1000 rpm bonnet rotational speed, and d) 1.0 mm bonnet offset and 2000 rpm bonnet rotational speed.

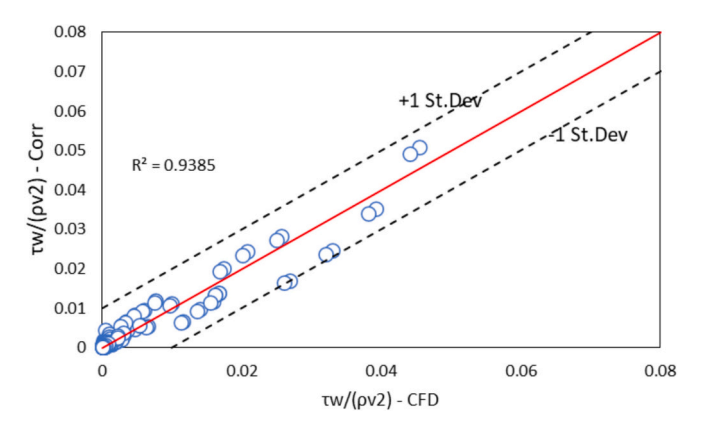


Fig. 16. Comparison between CFD dimensionless shear stress and the new correlation predictions.

Ameer Hussain: Writing – review & editing, Software, Investigation. David Walker: Project administration, Funding acquisition, Conceptualization. Xun Chen: Writing – review & editing. Paul A. Bingham: Writing – review & editing. Juan Ahuir-Torres: Writing – review & editing. Hongyu Li: Writing – review & editing.

Declaration of competing interest

The authors declare that they have no known competing financial interests or personal relationships that could have appeared to influence

the work reported in this paper.

Acknowledgements

The authors acknowledge the funding provided for this work by the Engineering and Physical Science Research Council (EPSRC), UK Grant number EP/V029304/1, EP/V029266/1, EP/V029274/1 and EP/V029401/1.

References

- Ghosh G, Sidpara A, Bandyopadhyay P. Fabrication of optical components by ultraprecision finishing processes. In: Micro and precision manufacturing; 2018.
- [2] Yadav HNS, Das M. Advances in finishing of optical complex substrates: a comprehensive review. Opt Laser Technol 2024;176:110938.
- [3] Walker DD, et al. The 'precessions' tooling for polishing and figuring flat, spherical and aspheric surfaces. Opt Express 2003;11(8):958-64.
- [4] Cook LM. Chemical processes in glass polishing. J Non-Cryst Solids 1990;120(1–3): 152–71
- [5] Kaufman F, et al. Chemical-mechanical polishing for fabricating patterned W metal features as chip interconnects. J Electrochem Soc 1991;138(11):3460.
- [6] Abiade JT, Yeruva S, Choi W, Moudgil BM, Kumar D, Singh RK. A tribochemical study of ceria-silica interactions for CMP. J Electrochem Soc 2006;153(11):G1001.
- [7] Zhao Y, Chang L, Kim S. A mathematical model for chemical–mechanical polishing based on formation and removal of weakly bonded molecular species. Wear 2003; 254(3–4):332–9.
- [8] Xin J, Cai W, Tichy J. A fundamental model proposed for material removal in chemical–mechanical polishing. Wear 2010;268(5–6):837–44.
- [9] Heisel U, Avroutine J. Process analysis for the evaluation of the surface formation and removal rate in lapping. CIRP Ann 2001;50(1):229–32.
- [10] Marinescu I, Shoutak A, Spanu CE. Technological assessment of double side lapping of silicon. 12/01/2001. p. 5–9.
- [11] Li B, Guo X, Liu Y, Li B, Wang D, Shen G. Study on the back lapping and polishing of sapphire-based LED epitaxial wafers. Semicond Technol 2005;30(9):57–60.

- [12] Othman MK, Dolah A, Omar NA, Yahya MR. Design of experiment (DOE) for thickness reduction of GaAs wafer using lapping process. In: 2006 IEEE international conference on semiconductor electronics. IEEE; 2006. p. 583–5.
- [13] Wang Z, Wu Y, Dai Y, Li S. Subsurface damage distribution in the lapping process. Appl Opt 2008;47(10):1417–26.
- [14] Rabinowicz E, Dunn L, Russell P. A study of abrasive wear under three-body conditions. Wear 1961;4(5):345–55.
- [15] Forsberg M. Effect of process parameters on material removal rate in chemical mechanical polishing of Si (1 0 0). Microelectron Eng 2005;77(3-4):319-26.
- [16] Guo J, Suzuki H. Effects of process parameters on material removal in vibrationassisted polishing of micro-optic mold. Micromachines 2018;9(7):349.
- [17] Larsen-Badse J. Influence of grit diameter and specimen size on wear during sliding abrasion. Wear 1968;12(1):35–53.
- [18] Malkin S, Wiggins K, Osman M, Smalling R. Size effects in abrasive processes. In: Proceedings of the thirteenth international machine tool design and research conference. Springer; 1973. p. 291–6.
- [19] Sin H, Saka N, Suh N. Abrasive wear mechanisms and the grit size effect. Wear 1979;55(1):163–90.
- [20] Misra A, Finnie I. On the size effect in abrasive and erosive wear. Wear 1981;65(3):
- [21] Kosel T, Li S, Rao C. The size effect in abrasion of dual-phase alloys. ASLE Trans 1985;28(3):343–50.
- [22] Chandrasekaran T, Kishore. Grinding abrasive wear and associated particle size effect. Mater Sci Technol 1992;8(8):722–8.
- [23] Forrest D, Matsuoka K, Tse M-K, Rabinowicz E. Accelerated wear testing using the grit size effect. Wear 1993;162:126–31.
- [24] Gåhlin R, Jacobson S. The particle size effect in abrasion studied by controlled abrasive surfaces. Wear 1999;224(1):118–25.

- [25] Wu L, Ek M, Song M, Sichen D. The effect of solid particles on liquid viscosity. Steel Res Int 2011;82(4):388–97.
- [26] Wang X, Zhou D, Zhu G, Guo C. Rheological properties of two high polymers suspended in an abrasive slurry jet. e-Polymers 2021;21(1):186–93.
- [27] Asim T, Mishra R, Kollar LE, Pradhan SR. Optimal sizing and life-cycle cost modelling of pipelines transporting multi-sized solid–liquid mixtures. Int J Press Vessel Pip 2014;113:40–8.
- [28] Kumar U, Mishra R, Singh S, Seshadri V. Effect of particle gradation on flow characteristics of ash disposal pipelines. Powder Technol 2003;132(1):39–51.
- [29] Mishra R, Singh S, Seshadri V. Pressure drop across conventional and divergingconverging pipe bends in the flow of multi-sized particulate slurries. 1998.
- [30] Mishra R, Singh SN, Seshadri V. Study of wear characteristics and solid distribution in constant area and erosion-resistant long-radius pipe bends for the flow of multisized particulate slurries. Wear 1998;217(2):297–306. 1998/05/15, https://doi.org/10.1016/S0043-1648(98)00147-1.
- [31] Seshadri V, Singh S, Fabien C, Mishra R. Hold-up in multi-sized particulate solid-liquid flow through horizontal pipes. 2001.
- [32] Menter FR. Two-equation eddy-viscosity turbulence models for engineering applications. AIAA J 1994;32(8):1598–605.
- [33] Walker D, et al. Bridging the divide between iterative optical polishing and automation. Nanomanuf Metrol 2023;6(1):26.
- [34] Lun C, Savage SB, Jeffrey D, Chepurniy N. Kinetic theories for granular flow: inelastic particles in Couette flow and slightly inelastic particles in a general flowfield. J Fluid Mech 1984;140:223–56.
- [35] Gidaspow D. Multiphase flow and fluidization: continuum and kinetic theory descriptions. Academic Press; 1994.